SHORT COMMUNICATION

Preparation of Regenerated Silk Fibroin Hybrid Fibers with Hydrogen Peroxide Sensing Properties by Wet Spinning

Song Lu[1], Jianjun Guo[2], Richard Ansah Herman[1], Xinyi Wu[1], Lin Ma[1] and Guohua Wu[1,*]

[1]College of Biotechnology, Jiangsu University of Science and Technology, Zhenjiang, 212100, China

[2]College of Agriculture, Anshun University, Anshun, 561000, China

[*]Corresponding Author: Guohua Wu. Email: ghwu@just.edu.cn

ABSTRACT

Silk is widely used in the production of high-quality textiles. At the same time, the amount of silk textiles no longer in use and discarded is increasing, resulting in significant waste and pollution. This issue is of great concern in many countries where silk is used. Hydrogen peroxide as a naturally occurring compound is an important indicator of detection in both biology and the environment. This study aims to develop a composite fiber with hydrogen peroxide-sensing properties using discarded silk materials. To achieve this goal, firstly, polydopamine (PDA) was used to encapsulate the $ZnFe_2O_4$ NPs to achieve the improvement of dispersion, and then regenerated silk fibroin (RSF) and $PDA@ZnFe_2O_4$/RSF hybrid fibers are prepared by wet spinning. Research has shown that $PDA@ZnFe_2O_4$/RSF demonstrates exceptional sensitivity, selectivity, and stability in detecting hydrogen peroxide, while maintaining high mechanical strength. Furthermore, the complete hybridization of $PDA@ZnFe_2O_4$ with silk fibroin not only results in the combination of the durability of silk fibroin and $PDA@ZnFe_2O_4$'s rigidity, ensuring a reliable service life, but also makes $PDA@ZnFe_2O_4$/RSF exhibit excellent catalytic activity and biocompatibility. Therefore, the composite fiber exhibits exceptional mechanical properties and reliable hydrogen peroxide sensing capabilities, making it a promising material for biological and medical applications.

KEYWORDS

Regenerated silk fibroin; modified zinc ferrite nanoparticles; composite fiber; hydrogen peroxide sensor; wet spinning

1 Introduction

Waste silk products have significant potential value and can be recycled to improve overall utilization [1]. The processing of silk products using RSF fibers can enhance their functional properties [2]. Silk proteins comprise the primary components of silk and exhibit exceptional physicochemical properties [3], including lightweight, softness, and high tensile strength. These characteristics make silk proteins highly promising for a wide range of applications in fields such as textiles [4], medicine [5], and biomaterials [6]. With the advancement of biotechnology and nanotechnology, scientists are employing techniques like genetic engineering to enhance silk fibroin, aiming to meet the demands of various industries. In the field of medicine, researchers have discovered that silk proteins exhibit outstanding biocompatibility and degradability, making them widely employed in the fabrication of biomedical materials, including sutures and tissue engineering for tissue repair [7]. Research on silk proteins plays a crucial role in driving

advancements in materials science, medicine, and biotechnology, offering new perspectives and avenues for creating more efficient and environmentally friendly materials and technologies for humanity [8]. However, research on its application in biosensors remains relatively scarce. Zinc ferrite nanoparticles ($ZnFe_2O_4$) represent a significant nanomaterial, characterized by their unique spinel-type microcrystalline structure and properties, which render them promising for a wide range of applications in magnetism [9], catalysis [10], biomedicine [11], and other fields. It exhibits outstanding performance in the field of catalysis. Its unique crystal structure and surface active sites make it an ideal choice for catalysts, widely utilized in organic synthesis and environmental purification [12,13]. As a catalyst, zinc ferrite nanoparticles not only demonstrate high catalytic activity but also exhibit exceptional stability and reusability. They hold tremendous potential in the field of magnetic materials. Its crystal structure and magnetic properties render it an ideal soft magnetic material [14], suitable for fabricating high-performance magnetic sensors, memory devices, and magnetic nanoparticles [15]. Additionally, it exhibits outstanding biocompatibility [16] and drug-delivery capabilities [17]. This makes it a promising functional material in areas such as tumor therapy, imaging diagnostics, and biosensing. Hydrogen peroxide (H_2O_2) stands as one of the most crucial substances analyzed today [18]. Sensors for detecting hydrogen peroxide (H_2O_2) are particularly significant, finding widespread applications in medicine [19], food safety [20], environmental monitoring [21], and other fields. Sensors are classified into enzyme sensors and nanoenzyme sensors based on the presence of enzymes [22]. Enzyme sensors are characterized by high catalytic activity and strong specificity. However, their low stability, susceptibility to variation, and high cost limit their practical applications. With the development of nanomaterials, nanoenzyme sensors have emerged as a focal point of research [23–25]. In recent years, researchers have delved into addressing the shortcomings of hydrogen peroxide sensors, leading to advancements in hydrogen peroxide colorimetric dish sensors [26]. Hydrogen peroxide colorimetric dish sensors utilize optical principles to reflect changes in hydrogen peroxide concentration through color variations. This approach simplifies detection steps and enhances sensitivity and real-time monitoring capabilities [27]. These sensors demonstrate significant potential in the medical field, as they can be employed for real-time monitoring of hydrogen peroxide concentration in physiological fluids, aiding in clinical diagnosis and disease treatment [28]. In food safety and environmental monitoring, these sensors also offer rapid and accurate detection of hydrogen peroxide content in samples, providing robust support for food quality inspection and environmental protection [29].

Poly-dopamine (PDA)-modified zinc ferrite ($ZnFe_2O_4$) nanoparticles were blended with silk fibroin (SF) using wet spinning to prepare a PDA@$ZnFe_2O_4$/RSF hybrid fiber. The cross-linking effect of PDA improved the dispersion of nanomaterials in silk fibroin and modified the properties of RSF. This resulted in the preparation of a PDA@$ZnFe_2O_4$/RSF hybrid with high sensitivity, selectivity, and stability.

2 Materials and Methods

2.1 Preparation of RSF Solution and PDA@ZnFe_2O_4/RSF Hybrid Fibers

The degummed silk was obtained by degumming discarded cocoon [30]. Add an appropriate amount of discarded cocoon to 0.05% Na_2CO_3 aqueous solution. Follow the bath ratio of 1:20 to boil for 30 min. Repeat this process three times. The degummed silk was dried at 45°C to constant weight. To obtain RSF solution with a 15% mass fraction, dissolve 1 g of desiccated silk in $CaCl_2$-FA solution [31]. A certain amount of $ZnFe_2O_4$ NPs was added to 0.1 M Tris-HCl buffer (pH 8.5) and sonicated for 30 min. Subsequently, dopamine, with a mass ratio of 10:1 to $ZnFe_2O_4$ NPs, was added to the same buffer and sonicated for another 30 min. The resulting mixture was stirred overnight (24 h) at a constant speed, followed by centrifugation at 12000 rpm for 30 min to remove the supernatant. This process of removing the supernatant and washing it with distilled water was repeated three times. The centrifuged product was then dried in a freeze-dryer for 24 h to obtain PDA@$ZnFe_2O_4$ NPs. As shown in Fig. 1a, synthesized PDA@$ZnFe_2O_4$ NPs were added to a 15 wt% degummed silk solution, with PDA@$ZnFe_2O_4$ NPs added in amounts corresponding to 0.2, 0.4, 0.6, 0.8, and 1.0 wt% relative to the mass fraction of degummed silk, respectively. The mixture was stirred at low speed for 4 h at room temperature. After stirring, the

spinning stock solution was obtained. Wet spinning was performed using a custom-made device, where the spinning solution was injected into a coagulation bath using a medical syringe. The coagulation bath was 1 meter long, and filled with 75% ethanol solution. The spinning solution was injected into the coagulation bath at a rate of 2 mL/h through a needle with a diameter of 0.21 mm attached to an injection pump. The spinning solution rapidly solidified into uniform fibers in the coagulation bath. The freshly spun fibers were collected and wound around a rotating shaft after undergoing stretching treatment. The collected PDA@ZnFe$_2$O$_4$/RSF hybrid fibers were immersed in a 75% ethanol solution for several hours to remove residual solvent and set. Finally, the PDA@ZnFe$_2$O$_4$/RSF hybrid fibers were removed and air-dried for 24 h. Table 1 lists the compositions of PDA@ZnFe$_2$O$_4$/RSF hybrid fibers at different concentrations of PDA@ZnFe$_2$O$_4$ NPs.

Table 1: Composition of RSF fibers and PDA@ZnFe$_2$O$_4$/RSF hybrid fibers

| Samples	Quality percentage (%)	
	PDA@ZnFe$_2$O$_4$ NPs	RSF
RSF fibers	0	100.00
0.2 wt% PDA@ZnFe$_2$O$_4$/RSF hybrid fibers	0.20	99.80
0.4 wt% PDA@ZnFe$_2$O$_4$/RSF hybrid fibers	0.40	99.60
0.6 wt% PDA@ZnFe$_2$O$_4$/RSF hybrid fibers	0.60	99.40
0.8 wt% PDA@ZnFe$_2$O$_4$/RSF hybrid fibers	0.80	99.20
1.0 wt% PDA@ZnFe$_2$O$_4$/RSF hybrid fibers	1.00	99.00

2.2 Characterization

The mechanical properties of PDA@ZnFe$_2$O$_4$/RSF were determined using an Instron 3343 single-fiber mechanical tensile tester (Instron, MA, USA). The surface morphology was observed using a scanning electron microscope (Hitachi SU-70, Tokyo, Japan). The crystallinity and grain size of PDA@ZnFe$_2$O$_4$/RSF were determined using the D8 DISCOVER model WAXD (Bruker, Kanisnhe, Germany). The characterization of PDA@ZnFe$_2$O$_4$/RSF was carried out using a Thermo Scientific Nicolet IS 10 Fourier transform infrared spectrometer (Thermo Fisher, MA, USA). The stability of PDA@ZnFe$_2$O$_4$/RSF was determined using a thermogravimetric analyzer (NETZSCH STA-2500, Bavaria, Germany). The sensing properties of PDA@ZnFe$_2$O$_4$/RSF were analyzed using a UV-2600 UV spectrophotometer (Shimadzu, Tokyo, Japan). Cytotoxicity experiments were carried out using an IX83 research-grade inverted microscope (OLYMPUS, Tokyo, Japan) and PerkinElmer EnSpire multifunctional enzyme labeler (PerkinElmer, Singapore) and CCK-8.

3 Results and Discussion

3.1 Topographic Analysis

The surface of 0.8 wt% PDA@ZnFe$_2$O$_4$/RSF hybrid fibers still exhibits a uniform and dense structure, with a slightly rough texture and low surface smoothness. There are no obvious cracks or pores observed on the cross-section. This indicates the good uniformity and compactness of the material synthesized, without any agglomeration, which meets the design requirements (Fig. 1b,c). In the EDS images, the presence of elements C, N, and O, which are constituents of silk fibroin, can be observed. Additionally, Fe and Zn elements are also detected, indicating successful modification of RSF fibers with PDA@ZnFe$_2$O$_4$ NPs, with good dispersion of PDA@ZnFe$_2$O$_4$ NPs within the RSF matrix (Fig. 1d–i). Fig. 1j displays the elemental content analysis of PDA@ZnFe$_2$O$_4$/RSF hybrid fibers, with carbon (C) content at 27.37%, nitrogen (N) content at 15.01%, oxygen (O) content at 56.10%, iron (Fe) content at 0.94%, and zinc (Zn) content at 1.58%.
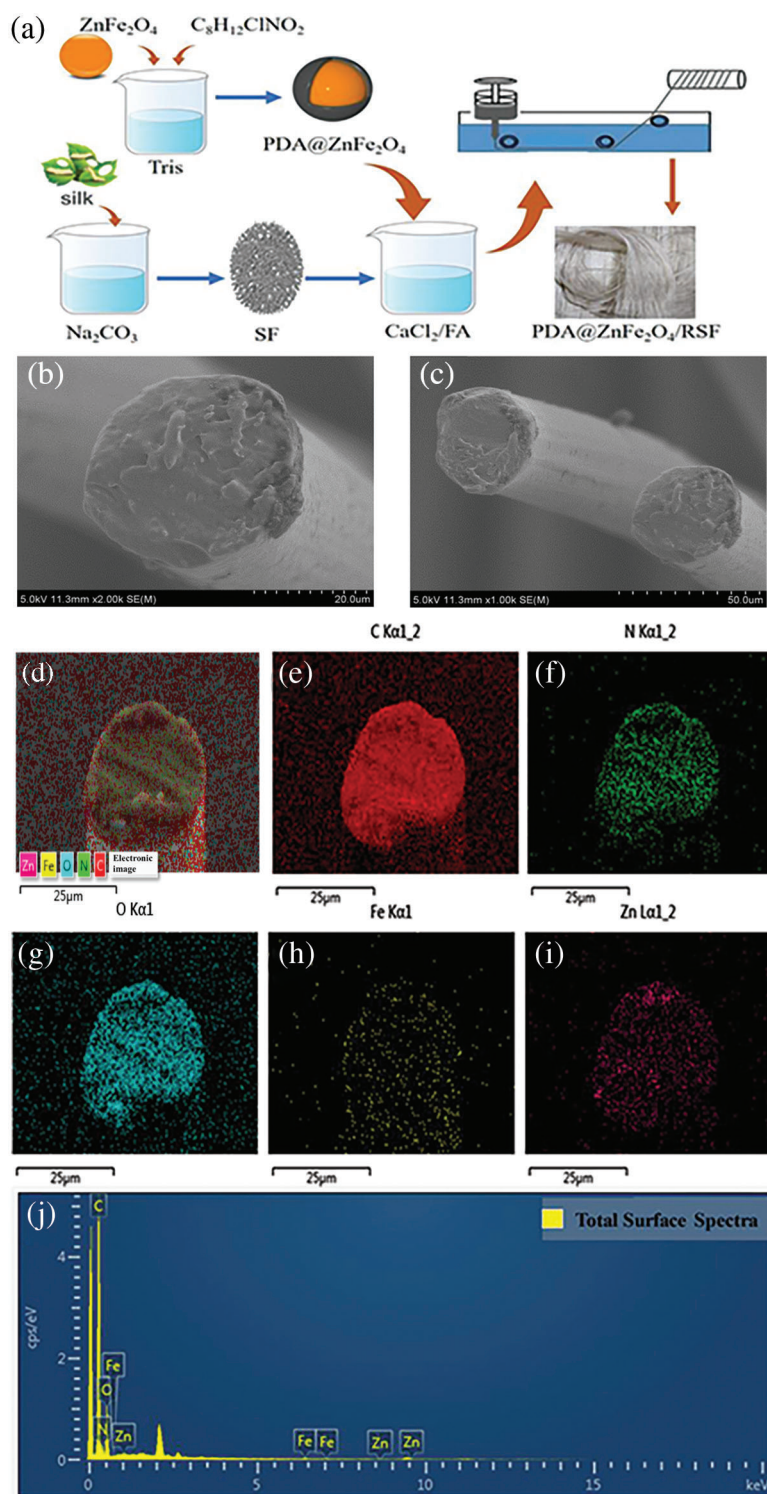
Figure 1: (a) Process flow diagram. Scanning electron microscope images: (b and c) display the cross-section and surface of PDA@ZnFe$_2$O$_4$/RSF hybrid fibers. Scale bars are 20 and 50 μm, respectively. Energy-dispersive X-ray spectroscopy (EDS) images of PDA@ZnFe$_2$O$_4$/RSF hybrid fibers: (d) Surface elemental distribution of PDA@ZnFe$_2$O$_4$/RSF hybrid fibers; (e) Distribution of carbon (C) elements; (f) Distribution of nitrogen (N) elements; (g) Distribution of oxygen (O) elements; (h) Distribution of iron (Fe) elements; (i) Distribution of zinc (Zn) elements. (j) Elemental analysis of PDA@ZnFe$_2$O$_4$/RSF hybrid fibers

3.2 Mechanical Properties and Secondary Structure

When the breaking strength of the PDA@ZnFe$_2$O$_4$/RSF hybrid fiber reaches its highest value, the content of PDA@ZnFe$_2$O$_4$ NPs is 0.8 wt% (Fig. 2a). The breaking strength is 287.1 MPa, and the elongation at break is 53.7%. The mechanical properties of the other groups have also shown improvement compared to the Control group. Analysis of the mechanical properties indicates that the addition of 0.8 wt% significantly enhances the mechanical properties of the hybrid fiber. Moreover, the incorporation of PDA@ZnFe$_2$O$_4$ NPs enhances the mechanical properties of groups other than the Control group to some extent.

The four characteristic peaks in Fig. 2c indicate that the hybrid fiber is not significantly different from the blank RSF fiber. Moreover, there are no new absorption peaks in the characteristic peaks of RSF, suggesting that the secondary structure of RSF remains unchanged by the addition of PDA@ZnFe$_2$O$_4$ NPs. The secondary structure of the hybrid fiber was analyzed using Peakfit software, As shown in Fig. 2b, the content of β-sheets in RSF fibers without PDA@ZnFe$_2$O$_4$ NPs addition is 29.58%. When the addition of PDA@ZnFe$_2$O$_4$ NPs is 0.8 wt%, the content of β-sheets in RSF hybrid fibers reaches the highest value of 36.36%. However, when the addition of PDA@ZnFe$_2$O$_4$ NPs is increased to 1 wt%, the content decreases to 33.32%. The trend of β-sheet change is initially an increase followed by a gradual decrease, which affects the fiber structure [32]. The optimal concentration of PDA@ZnFe$_2$O$_4$ NPs was determined to be 0.8 wt% based on their secondary structure and mechanical properties.

WAXD analysis was conducted on RSF fibers before and after hybridization to investigate the crystallinity, crystal size, and orientation relative to the macroscopic axis of the fibers. The 2D-WAXD patterns revealed characteristic diffraction rings typical of RSF in PDA@ZnFe$_2$O$_4$/RSF hybrid fibers. The addition of PDA@ZnFe$_2$O$_4$ NPs did not significantly affect the RSF fibers (Fig. 2d). Fig. 2e presents the results of peak fitting, with the three crystal planes (200), (210), and (002) corresponding to the a, b, and c axes of the crystal, respectively. The crystallinity and average crystal size were determined from the peak fitting. The addition of PDA@ZnFe$_2$O$_4$ NPs resulted in an increase in the crystallinity of RSF and a decrease in crystal volume, from the original 9.45 nm^3 and 38.41% to 7.93 nm^3 and 39.10%, respectively (Table 2).
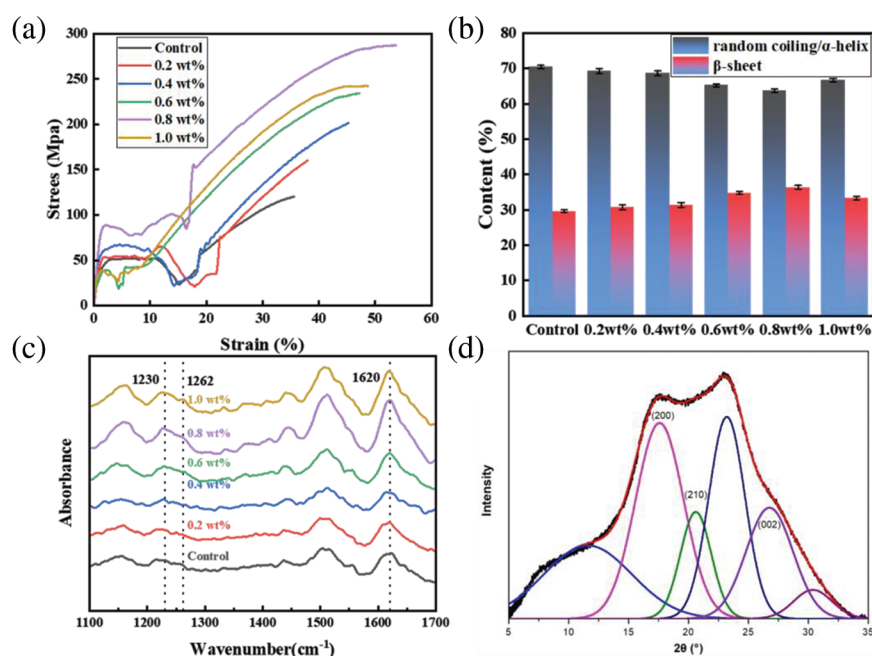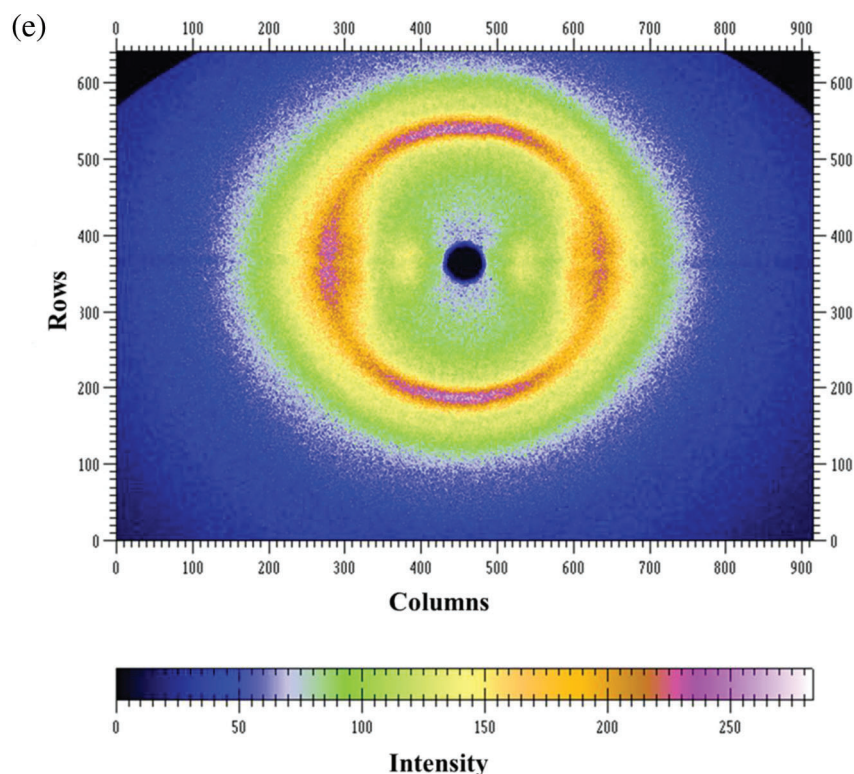

Figure 2: (Continued)

Figure 2: (a) Stress-strain curves of PDA@ZnFe$_2$O$_4$/RSF hybrid fibers with different concentrations of PDA@ZnFe$_2$O$_4$ NPs; (b) Secondary structure content; (c) Infrared spectra. (d) 2D-WAXD pattern of 0.8 wt% PDA@ZnFe$_2$O$_4$/RSF hybrid fibers. (e) WAXD pattern deconvolution of 0.8 wt% PDA@ZnFe$_2$O$_4$/RSF hybrid fibers

**Table 2:** The crystallinity and crystallite size of 0.8 wt% PDA@ZnFe$_2$O$_4$/RSF hybrid fibers

| Samples	Crystallite size (nm)				Crystallinity
	a	b	c	V/nm^3	
RSF fibers	1.72	2.58	2.13	9.45	38.41%
0.8 wt% PDA@ZnFe$_2$O$_4$/RSF hybrid fibers	1.69	2.65	1.77	7.93	39.10%

3.3 Hydrogen Peroxide Sensing Properties

Fig. 3 illustrates the catalytic reaction mechanism of PDA@ZnFe$_2$O$_4$/RSF for H$_2$O$_2$ sensing. The reaction conditions were optimized before the experiment (Fig. 4a–d) and the optimal conditions were determined: a reaction time of 40 min, a pH of 4, a temperature of 40°C, and a TMB concentration of 16 µg/mL.

To better explore the enzyme-like properties of 0.8 wt% PDA@ZnFe$_2$O$_4$/RSF, the steady-state kinetics of its performance as a nanozyme were investigated. Under optimal reaction conditions, typical Michaelis-Menten curves were obtained by fixing the concentration of one substrate (TMB and H$_2$O$_2$) while varying the concentration of the other substrate (H$_2$O$_2$ and TMB), as shown in Fig. 5a,b. Subsequently, Lineweaver-Burk plots were obtained through transformation and calculation, as

depicted in Figs. 5c (H_2O_2) and 5d (TMB). Utilizing the Lineweaver-Burk equation, the Michaelis constants (Km) and maximum reaction rates (Vmax) of 0.8 wt% PDA@ZnFe$_2$O$_4$/RSF as a nanozyme were calculated and are listed in Table 3. A comparison with other nanozymes was conducted. The results indicate that the Km value for H_2O_2 as a substrate is 0.30 mM, while the Km value for TMB as a substrate is 0.19 mM. These findings further demonstrate the excellent catalytic activity of 0.8 wt% PDA@ZnFe$_2$O$_4$/RSF.
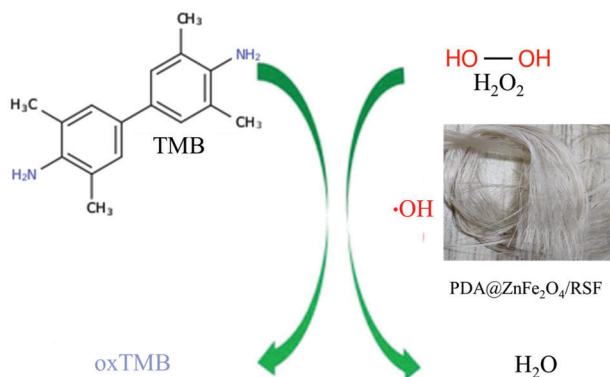
Figure 3: Illustrates the schematic diagram of the H_2O_2 colorimetric sensor based on PDA@ZnFe$_2$O$_4$/RSF
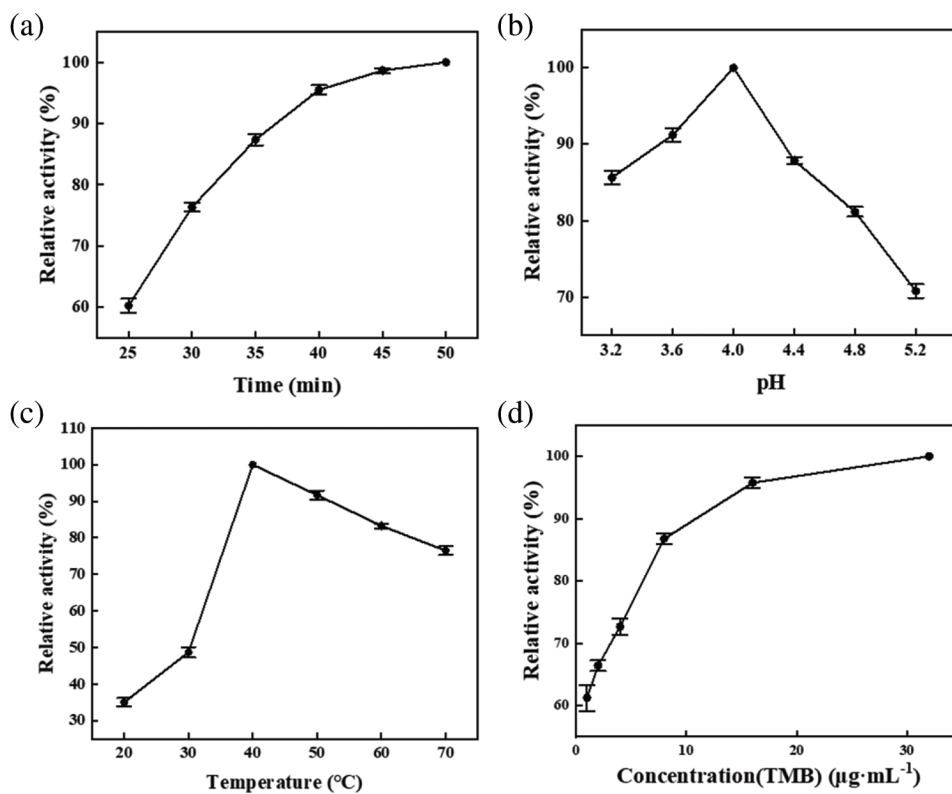
Figure 4: Reaction conditions: The influence of (a) time, (b) pH, (c) temperature, and (d) TMB concentration on the enzymatic activity of PDA@ZnFe$_2$O$_4$/RSF
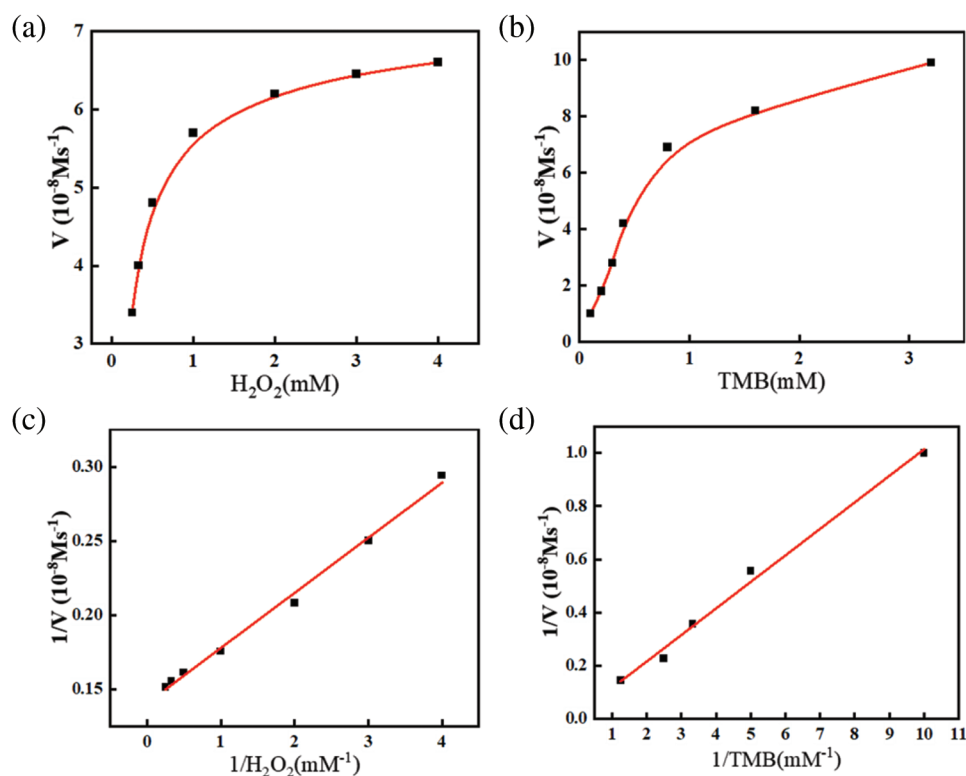
Figure 5: (a) Keeping TMB concentration at 4 mM while varying H_2O_2 concentration; (b) Keeping H_2O_2 concentration at 0.1 M while varying TMB concentration; (c) Lineweaver-Burk plot with varying H_2O_2 concentration; (d) Lineweaver-Burk plot with varying TMB concentration

Table 3: Comparison of kinetic parameters between PDA@ZnFe$_2$O$_4$/RSF and other nanoenzymes

Catalyst	Substrate	Km (mM)	Vmax ($10^{-8}Ms^{-1}$)	Reference
Fe$_3$O$_4$@CeO	TMB	0.15	0.64	[33]
	H$_2$O$_2$	1.13	12.5	
Fe-MIL-88NH$_2$	TMB	0.284	1.048	[34]
	H$_2$O$_2$	0.206	0.704	
Hemin@MIL-53(Al)-NH$_2$	TMB	0.068	0.607	[35]
	H$_2$O$_2$	10.9	0.898	
Co/Mn-MOFs-1-1-150	TMB	0.270	1.64	[36]
	H$_2$O$_2$	0.240	5.80	
PDA@ZnFe$_2$O$_4$/RSF	TMB	0.19	6.9	This work
	H$_2$O$_2$	0.30	10.3	

    The sensitivity of 0.8 wt% PDA@ZnFe$_2$O$_4$/RSF was first tested (Fig. 6a). Fig. 6b depicts the linear relationship between the absorbance values at 652 nm and the concentration of H_2O_2 corresponding to Fig. 6a. 0.8 wt% PDA@ZnFe$_2$O$_4$/RSF showed high sensitivity to unusual concentrations of H_2O_2 solution with different absorbance responses. It can be detected quickly and accurately even at low

concentrations. The additive equation A = 0.00385C + 0.22 (μM) describes the additive relationship between absorbance (A) and concentration (C), with a correlation coefficient of 0.99742 (n = 3) and the detection limit is 0.12 μM. Finally, comparison was made between 0.8 wt% PDA@ZnFe$_2$O$_4$/RSF and other nanozymes, as shown in Table 4. The results indicate that 0.8 wt% PDA@ZnFe$_2$O$_4$/RSF exhibits excellent linearity and detection limits.
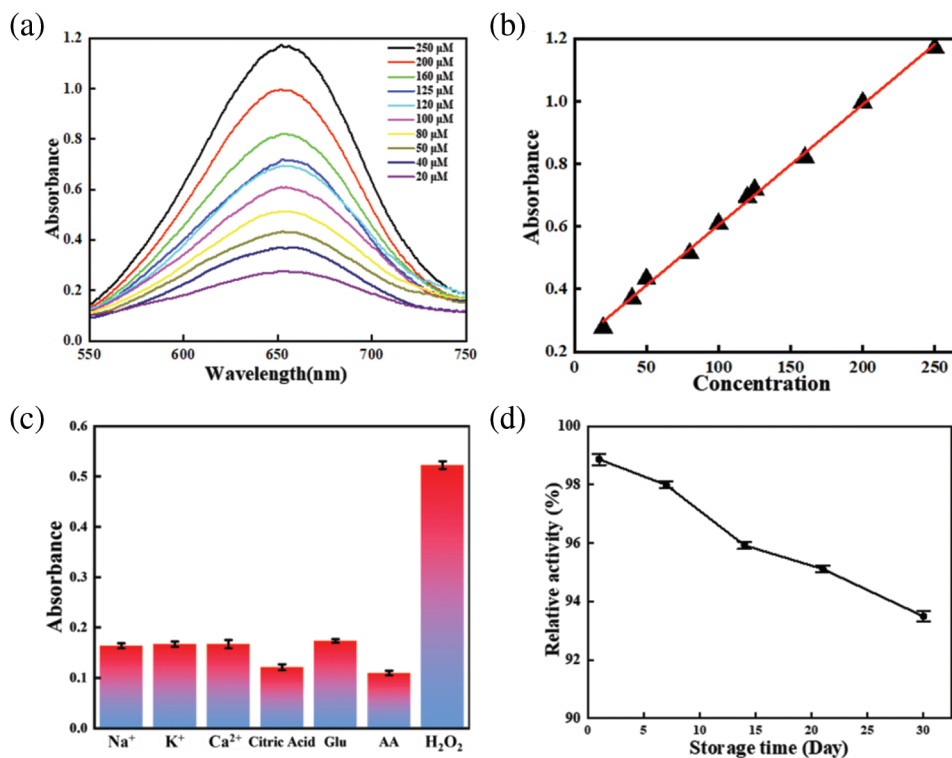
Figure 6: (a) UV-visible absorption spectra after reaction with different H$_2$O$_2$ concentrations; (b) linear calibration curve for H$_2$O$_2$. (c) Absorption values for the system in the presence of H$_2$O$_2$ and different interfering substances. (d) Peroxidase-like activity of PDA@ZnFe$_2$O$_4$/RSF over time

Table 4: Compare the linear range and detection limit of different H$_2$O$_2$ colorimetric sensors

Catalyst	Linear range	Detection limit	Reference
Fe$_3$O$_4$@MSN	1~100 μM	1 μM	[37]
Pal@Co$_3$O$_4$	1~60 μM	0.70 μM	[38]
PB/MIL-101(Fe)	2.4–100 μM	0.15 μM	[39]
TiO$_2$/MoS$_2$	0.05~1 μM	0.05 μM	[40]
PDA@ZnFe$_2$O$_4$/RSF	20~250 μM	0.12 μM	This work

In the selective assay (Fig. 6c), tests were conducted with various interfering substances (Na$^+$, K$^+$, Ca^{2+}, citric acid, AA, Glu) mixed with the target substance. The PDA@ZnFe$_2$O$_4$ NPs demonstrated high selectivity for the target substances. They accurately discriminated and responded to target substances amidst interfering substances, enabling precise detection of target substances in complex environments.

During the stability test (Fig. 6d) to assess the long-term stability performance of the material, the same batch of 0.8 wt% PDA@ZnFe$_2$O$_4$/RSF was used to measure the same concentration of H$_2$O$_2$ at five different time points (0, 1, 7, 14 and 30 d), respectively. By comparing changes in absorbance, it is able to maintain a better stability of performance during use. It exhibits good stability in practical applications, enabling continuous and accurate measurements.

3.4 Toxicity Analysis and Thermogravimetric Analysis

L929 and H9C9 cells were selected as experimental subjects in Fig. 7c,d. The toxic effects of RSF and 0.8 wt% PDA@ZnFe$_2$O$_4$/RSF were analysed at a concentration of 0.5 mg/mL. The results showed that both materials had very low toxicity to the cells, with a survival rate of over 90%, indicating a cell growth-promoting effect. This confirms the excellent biocompatibility and bioactivity of the 0.8 wt% PDA@ZnFe$_2$O$_4$/RSF in cells.
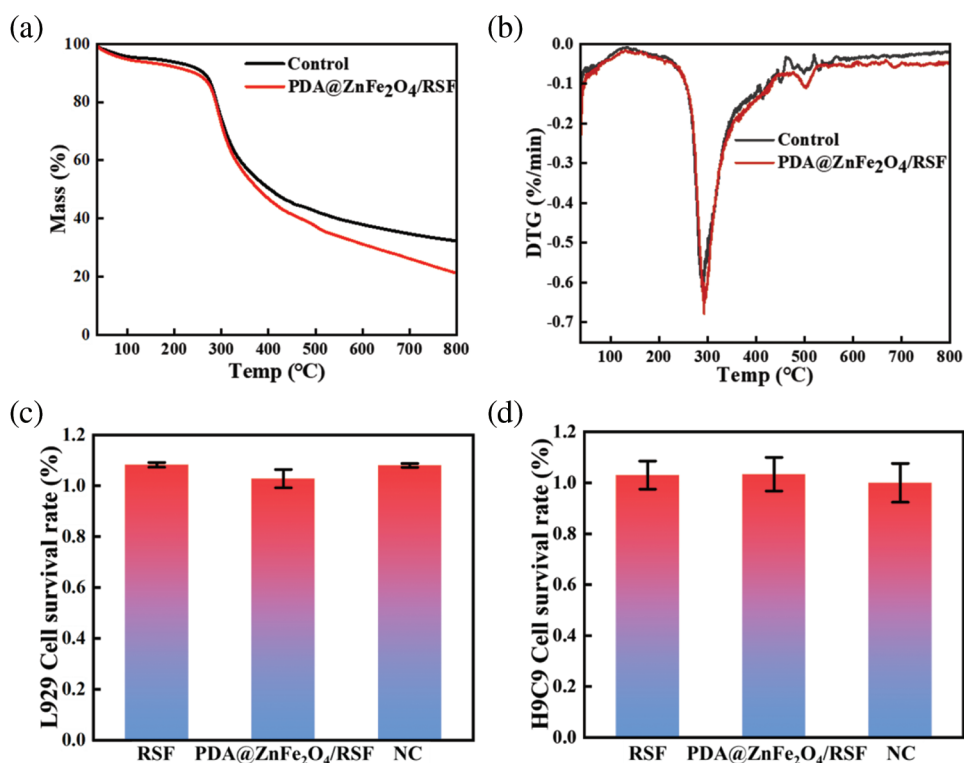
Figure 7: (a) TG curves of 0.8 wt% PDA@ZnFe$_2$O$_4$/RSF hybrid fibers and RSF fibers; (b) DTG curves of 0.8 wt% PDA@ZnFe$_2$O$_4$/RSF hybrid fibers and RSF fiber. (c) Cytotoxicity of PDA@ZnFe$_2$O$_4$/RSF hybrid fibers and RSF fibers on L929 cells. (d) Cytotoxicity of PDA@ZnFe$_2$O$_4$/RSF hybrid fibers and RSF fibers on L929 cells

Thermogravimetric analysis (TGA) of 0.8 wt% PDA@ZnFe$_2$O$_4$/RSF (Fig. 7a,b) revealed a significant mass change. This mass change is attributed to the presence of iron in 0.8 wt% PDA@ZnFe$_2$O$_4$/RSF, which undergoes thermal decomposition, oxidation, and other reactions, resulting in a gradual decrease in mass during the warming process. The substantial decrease in the material's mass suggests that 0.8 wt% PDA@ZnFe$_2$O$_4$/RSF exhibits high thermal activity and reactivity. Thermo-gravimetric analysis provides valuable insights into the thermal properties of 0.8 wt% PDA@ZnFe$_2$O$_4$/RSF, with blank experiments serving as benchmarks for comparison and eliminating systematic errors. The 0.8 wt% PDA@ZnFe$_2$O$_4$/RSF

composite demonstrates exceptional thermal activity, which translates into outstanding catalytic performance and thermochemical properties. Consequently, it is well-suited for applications in the field of nanoenzymes. Its unique characteristics enable efficient catalysis of various reactions and excellent performance under different thermal conditions.

4 Conclusions

The PDA@ZnFe$_2$O$_4$/RSF hybrid fiber prepared by wet spinning in this study retained the physical and chemical structure and biocompatibility of RSF. The addition of PDA@ZnFe$_2$O$_4$ NPs improved significantly the mechanical strength and durability of the hybrid fibers. The hybrid fiber showed the best mechanical properties when the PDA@ZnFe$_2$O$_4$ NPs content was 0.8 wt%. In addition, the utilization of PDA@ZnFe$_2$O$_4$ NPs improves the properties of hybrid fibers, resulting in exceptional hydrogen peroxide sensors that exhibit high sensitivity, selectivity, and stability. This not only provides new ideas for the recycling of waste silk textiles but also provides new composite fiber materials with good application prospects for medical treatment and pollutant detection. The potential of the hybrid fiber in specific medical and environmental monitoring fields will be thoroughly investigated to enhance its practical application.

Author Contributions: The authors confirm their contribution to the paper as follows: study conception and design: Song Lu, Guohua Wu, Jianjun Guo; data collection: Xinyi Wu, Lin Ma; analysis and interpretation of results: Song Lu, Jianjun Guo; draft manuscript preparation: Song Lu, Richard Ansah Herman, Guohua Wu. All authors reviewed the results and approved the final version of the manuscript.

Availability of Data and Materials: The raw data required to reproduce these findings can be obtained upon request to ghwu@just.edu.cn.

Conflicts of Interest: The authors declare that they have no conflicts of interest to report regarding the present study.

References

1. Lu L, Fan W, Ge S, Liew RK, Shi Y, Dou H, et al. Progress in recycling and valorization of waste silk. Sci Total Environ. 2022;830:154812. doi:10.1016/j.scitotenv.2022.154812.

2. Tao H, Kaplan DL, Omenetto FG. Silk materials–a road to sustainable high technology. Adv Mater. 2012;24(21):2824–37. doi:10.1002/adma.201104477.

3. Strassburg S, Zainuddin S, Scheibel T. The power of silk technology for energy applications. Adv Energy Mater. 2021;11(43):2100519. doi:10.1002/aenm.v11.43.

4. Guan J, Huang ZN, Zou J, Jiang XY, Peng DM, Yu J, et al. A sensitive non-enzymatic electrochemical sensor based on acicular manganese dioxide modified graphene nanosheets composite for hydrogen peroxide detection. Ecotoxicol Environ Saf. 2020;190:110123. doi:10.1016/j.ecoenv.2019.110123.

5. Lujerdean C, Baci GM, Cucu AA, Dezmirean DS. The contribution of silk fibroin in biomedical engineering. Insects. 2022;13(3):286. doi:10.3390/insects13030286.

6. DeBari MK, King CI III, Altgold TA, Abbott RD. Silk fibroin as a green material. ACS Biomater Sci Eng. 2021;7(8):3530–44. doi:10.1021/acsbiomaterials.1c00493.

7. Holland C, Numata K, Rnjak-Kovacina J, Seib FP. The biomedical use of silk: past, present, future. Adv Healthc Mater. 2019;8(1):1800465. doi:10.1002/adhm.v8.1.

8. Guo J, Yang B, Ma Q, Fometu SS, Wu G. Photothermal regenerated fibers with enhanced toughness: silk fibroin/ MoS2 nanoparticles. Polymers. 2021;13(22):3937. doi:10.3390/polym13223937.

9. Rani BJ, Ravi G, Yuvakkumar R, Ganesh V, Ravichandran S, Thambidurai M, et al. Pure and cobalt-substituted zinc-ferrite magnetic ceramics for supercapacitor applications. Appl Phys A. 2018;124:1–12.

10. Amiri M, Eskandari K, Salavati-Niasari M. Magnetically retrievable ferrite nanoparticles in the catalysis application. Adv Colloid Interf Sci. 2019;271:101982. doi:10.1016/j.cis.2019.07.003.

11. Huang X, Chen Z, Yang R, Feng G. Facile preparation of dopamine-modified magnetic zinc ferrite immobilized lipase for highly efficient synthesis of OPO functional lipid. J Renew Mater. 2023;11(5):2301–19. doi:10.32604/jrm.2023.025888.

12. Erfaninia N, Tayebee R, Foletto E, Amini M, Dusek M, Zonoz F. Preparation of magnetically recyclable $ZnFe_2O_4$ nanoparticles by easy single-step co-precipitation method and their catalytic performance in the synthesis of 2-aminothiophenes. Appl Organomet Chem. 2018;32(2):e4047. doi:10.1002/aoc.v32.2.

13. Sharma S, Dutta V, Raizada P, Hosseini-Bandegharaei A, Thakur V, Nguyen VH, et al. An overview of heterojunctioned $ZnFe_2O_4$ photocatalyst for enhanced oxidative water purification. J Environ Chem Eng. 2021;9(5):105812. doi:10.1016/j.jece.2021.105812.

14. Mandal S, Natarajan S, Tamilselvi A, Mayadevi S. Photocatalytic and antimicrobial activities of zinc ferrite nanoparticles synthesized through soft chemical route: a magnetically recyclable catalyst for water/wastewater treatment. J Environ Chem Eng. 2016;4(3):2706–12. doi:10.1016/j.jece.2016.05.020.

15. Shaikh SF, Ubaidullah M, Mane RS, Al-Enizi AM. Types, synthesis methods and applications of ferrites. In: Spinel ferrite nanostructures for energy storage devices. Elsevier; 2020. p. 51–82.

16. Haghniaz R, Rabbani A, Vajhadin F, Khan T, Kousar R, Khan AR, et al. Anti-bacterial and wound healing-promoting effects of zinc ferrite nanoparticles. J Nanobiotechnol. 2021;19:1–15.

17. Zamani M, Naderi E, Aghajanzadeh M, Naseri M, Sharafi A, Danafar H. Co1-XZnxFe2O4 based nanocarriers for dual-targeted anticancer drug delivery: synthesis, characterization and in vivo and in vitro biocompatibility study. J Mol Liq. 2019;274:60–7. doi:10.1016/j.molliq.2018.10.083.

18. Chen S, Yuan R, Chai Y, Hu F. Electrochemical sensing of hydrogen peroxide using metal nanoparticles: a review. Microchim Acta. 2013;180:15–32. doi:10.1007/s00604-012-0904-4.

19. MoBhammer M, Kuhl M, Koren K. Possibilities and challenges for quantitative optical sensing of hydrogen peroxide. Chemosensors. 2017;5(4):28. doi:10.3390/chemosensors5040028.

20. Chen H, Zhou K, Zhao G. Gold nanoparticles: from synthesis, properties to their potential application as colorimetric sensors in food safety screening. Trends Food Sci Technol. 2018;78:83–94. doi:10.1016/j.tifs.2018.05.027.

21. Teodoro KB, Migliorini FL, Christinelli WA, Correa DS. Detection of hydrogen peroxide (H_2O_2) using a colorimetric sensor based on cellulose nanowhiskers and silver nanoparticles. Carbohydr Polym. 2019;212:235–41. doi:10.1016/j.carbpol.2019.02.053.

22. Xing L, Zhang W, Fu L, Lorenzo JM, Hao Y. Fabrication and application of electrochemical sensor for analyzing hydrogen peroxide in food system and biological samples. Food Chem. 2022;385:132555. doi:10.1016/j.foodchem.2022.132555.

23. Wang Q, Wei H, Zhang Z, Wang E, Dong S. Nanozyme: an emerging alternative to natural enzyme for biosensing and immunoassay. Trends Anal Chem. 2018;105:218–24. doi:10.1016/j.trac.2018.05.012.

24. Wang H, Wan K, Shi X. Recent advances in nanozyme research. Adv Mater. 2019;31(45):1805368. doi:10.1002/adma.v31.45.

25. Unnikrishnan B, Lien CW, Chu HW, Huang CC. A review on metal nanozyme-based sensing of heavy metal ions: challenges and future perspectives. J Hazard Mater. 2021;401:123397. doi:10.1016/j.jhazmat.2020.123397.

26. Liang A, Zhao Y, Huang X, Jiang Z. A facile and sensitive fluorescence assay for glucose via hydrogen peroxide based on MOF-Fe catalytic oxidation of TMB. Spectrochim Acta Part A: Mol Biomol Spectrosc. 2022;265:120376. doi:10.1016/j.saa.2021.120376.

27. Olgun FAO, Uzer A, Ozturk BD, Apak RJT. A novel cerium oxide nanoparticles–based colorimetric sensor using tetramethyl benzidine reagent for antioxidant activity assay. Talanta. 2018;182:55–61. doi:10.1016/j.talanta.2018.01.047.

28. Hou J, Qian M, Zhao H, Li Y, Liao Y, Han G, et al. A near-infrared ratiometric/turn-on fluorescent probe for in vivo imaging of hydrogen peroxide in a murine model of acute inflammation. Anal Chim Acta. 2018;1024:169–76. doi:10.1016/j.aca.2018.03.028.

29. Chen Q, Lin T, Huang J, Chen Y, Guo L, Fu F. Colorimetric detection of residual hydrogen peroxide in soaked food based on Au@ Ag nanorods. Anal Methods. 2018;10(5):504–7. doi:10.1039/C7AY02819A.

30. Wang L, Luo Z, Zhang Q, Guan Y, Cai J, You R, et al. Effect of degumming methods on the degradation behavior of silk fibroin biomaterials. Fibers Polymers. 2019;20:45–50. doi:10.1007/s12221-019-8658-9.

31. Yue X, Zhang F, Wu H, Ming J, Fan Z, Zuo B. A novel route to prepare dry-spun silk fibers from $CaCl_2$–formic acid solution. Mater Lett. 2014;128:175–8. doi:10.1016/j.matlet.2014.04.116.

32. Yazawa K, Hidaka K. Pressure-and humidity-induced structural transition of silk fibroin. Polymer. 2020;211:123082. doi:10.1016/j.polymer.2020.123082.

33. Huang FF, Wang J, Chen W, Wan Y, Wang X, Cai N, et al. Synergistic peroxidase-like activity of CeO_2-coated hollow Fe_3O_4 nanocomposites as an enzymatic mimic for low detection limit of glucose. J Taiwan Inst Chem Eng. 2017;83:40–9.

34. Liu YL, Zhao XJ, Yang XX, Li YF. A nanosized metal-organic framework of Fe-MIL-88NH_2 as a novel peroxidase mimic used for colorimetric detection of glucose. Analyst. 2013;138(16):4526–31. doi:10.1039/c3an00560g.

35. Qin FX, Sy Jia, Wang F, Sh Wu, Song J, Liu Y. Hemin@metal organic framework with peroxidase-like activity and its application to glucose detection. Catal Sci Tech. 2013;3:2761–8. doi:10.1039/c3cy00268c.

36. Qi X, Tian H, Dang X, Fan Y, Zhang Y, Zhao H. A bimetallic Co/Mn metal–organic-framework with a synergistic catalytic effect as peroxidase for the colorimetric detection of H_2O_2. Anal Methods. 2019;11(8):1111–24. doi:10.1039/C8AY02514B.

37. Wang Y, Zhou B, Wu S, Wang K, He X. Colorimetric detection of hydrogen peroxide and glucose using the magnetic mesoporous silica nanoparticles. Talanta. 2015;134:712–7. doi:10.1016/j.talanta.2014.12.013.

38. Chen P, Zhong H, Li XR, Li M, Zhou S. Palygorskite@ Co_3O_4 nanocomposites as efficient peroxidase mimics for colorimetric detection of H_2O_2 and ascorbic acid. Appl Clay Sci. 2021;209:106109. doi:10.1016/j.clay.2021.106109.

39. Cui F, Deng Q, Li S. Prussian blue modified metal-organic framework MIL-101(Fe) with intrinsic peroxidase-like catalytic activity as a colorimetric biosensing platform. RSC Adv. 2015;5:98215–21. doi:10.1039/C5RA18589K.

40. Zhu W, Chi M, Gao M, Wang C, Lu X. Controlled synthesis of titanium dioxide/molybdenum disulfide core-shell hybrid nanofibers with enhanced peroxidase-like activity for colorimetric detection of glutathione. J Colloid Interface Sci. 2018;528:410–8. doi:10.1016/j.jcis.2018.05.068.